

# 5

## The radiative forcing due to clouds and water vapor

V. RAMANATHAN AND ANAND INAMDAR

*Center for Atmospheric Sciences, Scripps Institution of Oceanography, University of California, San Diego, CA*

### 5.1 Introduction

As the previous chapters have noted, the climate system is forced by a number of factors, e.g., solar impact, the greenhouse effect, etc. For the greenhouse effect, clouds, water vapor, and CO<sub>2</sub> are of the utmost importance. The emergence of computers as a viable scientific tool in the 1960s in conjunction with the availability of spectroscopic data enabled us to treat the numerous complexities of infrared-radiative transfer in the atmosphere. While such calculations set the stage for estimating accurately (decades later in the 1990s) the radiative forcing due to greenhouse gases and clouds, they did not yield the necessary insights into the physics of the problem nor did they yield any explanation of the relevant phenomenon. Such insights needed physically based analytic approaches to the problem. It is in this arena that Dr. Robert Cess excelled and provided the community with important insights into numerous radiative processes in the atmosphere of Earth and other planets including Mars, Venus, Jupiter, and Saturn. A few examples that are relevant to the main theme of this chapter are given below.

Within the lower atmosphere of many planets (first 10 km of Earth; 5 km for Mars; and 60 km for Venus) the greenhouse effect is dominated by pressure-broadened vibration–rotational lines (e.g., CO<sub>2</sub> and CH<sub>4</sub>) or pure rotational lines (H<sub>2</sub>O) of polyatomic gases. Typically, the absorption and emission of radiation occurs in discrete bands with thousands of rotational lines within each band. Even with modern day supercomputers it is impossible to estimate the radiative transfer due to all of these lines and bands through the atmosphere for the entire planet. Thus a three-dimensional characterization of the radiative heating rates from equator to pole using the line-by-line approach is impractical. What is normally done is to use

so-called band models that approximate the effects of the thousands of lines with an equivalent line. Numerous scientists contributed to this important development (see Goody, 1964 for the details). Cess pioneered the development and, more importantly, the use of such band models (Cess and Tiwari, 1972) for understanding the thermal structure of planetary atmospheres (Cess, 1971; Cess and Khetan, 1973) in radiative as well as in radiative-convective equilibrium. For a CO<sub>2</sub>-dominant atmosphere (such as Mars and Venus), he gave the first analytical solutions for the integro-differential equation and obtained the vertical thermal structure of Mars and Venus (Cess and Ramanathan, 1972; Cess, 1982). This solution revealed many important insights that evaded most numerical solutions. It showed that under radiative-convective equilibrium, the temperature should be continuous across the tropopause, provided the line center is optically thick even if the opacity in the line wings is small. This is always the case for CO<sub>2</sub> in Mars and Venus and for H<sub>2</sub>O and CO<sub>2</sub> on Earth. The line-wing opacity, however, determines the location of the tropopause and the lower stratospheric temperature, for two reasons: First, the line center occupies only a minor fraction of the total band width, while the wings occupy more than 90% of the total band width; and second, the line-center optical depth is almost independent of pressure (i.e., altitude) (for a uniform mixed gas such as CO<sub>2</sub>), whereas the line-wing optical depth scales as square of the pressure. As a result, the line-wing opacity decreases rapidly with altitude. Thus the vertical variation of the line-wing optical depth dominates the vertical gradient of fluxes and the temperature.

Using these techniques developed for planets, Cess (1974; 1976) studied the greenhouse effect of H<sub>2</sub>O in Earth's atmosphere. He elucidated the role of clouds in regulating the water-vapor greenhouse effect. For example, Cess showed that fixing cloud altitude, as opposed to fixing cloud temperature, had a large effect on climate sensitivity to CO<sub>2</sub> doubling. He was one of the earliest to recognize the fundamental implication of the radiative-convective equilibrium assumption, i.e., the global temperature change can be determined by the radiative forcing at the top of the atmosphere, TOA (Cess, 1975). He brought his analytical skills in radiative transfer to guide the development of the Earth Radiation Budget Experiment (ERBE), one of NASA's successful climate missions. This experiment yielded a global and regional perspective of the radiative forcing due to clouds (e.g. Ramanathan *et al.*, 1989; Harrison *et al.*, 1990), and the greenhouse effect of the atmosphere (Raval and Ramanathan 1989), and settled many of the debates regarding the role of clouds in climate. One primary reason for the major role of ERBE is the fact that it undertook one of the most exhaustive and careful calibration and instrument-characterization efforts to date under the guidance of Cess along with ERBE project scientist Bruce Barkstrom. Employing a remarkably insightful and simple analytical procedure, Cess *et al.* (1989) used the ERBE cloud-forcing

and clear-sky greenhouse effect for validating the performance of over 10 general circulation models (GCMs) developed by various institutions around the world. This study conducted in the early 1990s (Cess *et al.*, 1990) revealed cloud feedback to be the major source of model differences in climate sensitivity and established cloud feedback as a major focus of research.

In this chapter, we use ERBE results to summarize our understanding of the radiative forcing due to water vapor and clouds. We begin with a historical perspective.

## 5.2 A historical perspective

### 5.2.1 Evolution of the greenhouse theory

The origins of the concept of the atmospheric greenhouse effect can be traced back to Jean-Baptiste Joseph Fourier (1827). He realized, almost two centuries ago, that the atmosphere is relatively transparent to solar radiation, but highly absorbent to the terrestrial radiation, thus helping to maintain a higher temperature for Earth's surface. A few decades later, John Tyndall (1861), using results from his detailed laboratory experiments, deduced that water vapor is the dominant gaseous absorber of infrared radiation.

However, it was S. Arrhenius (1896) who laid the formal foundation linking atmospheric gases to climate change. His main goal was to estimate the surface-temperature increase due to an increase in CO<sub>2</sub>. To this end, he developed a detailed and quantitative model for the radiation budget of the atmosphere and surface. Chamberlin (1899) also should get a major credit for this development. Arrhenius recognized the importance of water vapor in determining the sensitivity of climate to external forcing such as increase in CO<sub>2</sub> and solar insolation. A simple explanation for the water-vapor feedback among the early studies of climate sensitivity was the fact that the relative humidity of the atmosphere is invariant to climate change. As Earth warmed, the saturation vapor pressure ( $e_s$ ) would increase exponentially with temperature according to the Clausius–Clapeyron relation, and the elevated ( $e_s$ ) would (if relative humidity remains the same) enhance the water-vapor concentration, further amplifying the greenhouse effect. Although it is well known that atmospheric circulation plays a big role, a satisfactory answer as to why the relative humidity in the atmosphere is conserved is still elusive. Möller (1963) used the assumption of constant relative humidity and obtained a surprisingly large sensitivity for the surface temperature. The flaws of the surface-balance approach followed by Möller and others preceding him were illustrated by Syukuro Manabe and his collaborators. In a series of studies (Manabe and Strickler, 1964; Manabe and Wetherald, 1967), they employed a one-dimensional radiative-convective model using a global mean atmosphere, which included both radiative

and convective heat exchanges between Earth's surface and the atmosphere. Their study clearly illustrated that the radiative energy balance of the surface–atmosphere system is the fundamental quantity that governs global mean surface temperature. This finding, perhaps, provided much of the motivation for satellite-radiation budget studies, measuring the radiative fluxes at the top of the atmosphere from which we can deduce the radiative forcing of the surface–atmosphere system.

### ***5.2.2 Development of quantum theory and spectroscopy***

John Tyndall measured the heat absorption by gases ( $\text{CO}_2$  and  $\text{H}_2\text{O}$ ) through carefully designed experiments in the laboratory. Based on the results of these experiments, he concluded in his Bakerian lecture (Tyndall, 1861, p. 273–285), that the chief influence on terrestrial rays is exercised by the aqueous vapor, every variation of which must produce a climate change. His laboratory measurements were extended and supplemented by direct observations of atmospheric transmission by others during the following 30 years; the most important and reliable of such atmospheric data were taken by Samuel P. Langley (1834–1906). Langley (1884; 1889) designed a high precision thermal detector, the bolometer, and recorded numerous observations of the lunar and solar spectra. He recorded both the broadband radiance and the spectral radiance in about 20 spectral bands between 0.9 and 30  $\mu\text{m}$ . Langley's data enabled Arrhenius to attempt his pioneering calculation. The wavelength-dependence of the line absorption and the complexity of the radiative transfer in an inhomogeneous atmosphere were not included by Arrhenius, for these physics awaited the discovery of quantum mechanics. The birth of the quantum mechanical theory in the early twentieth century heralded the beginning of the theoretical and experimental spectroscopy, eventually leading to the availability of improved spectroscopic data (Goody, 1964).

Quantum theory postulated that infrared absorption and emission of thermal radiation result from molecular transitions involving both vibrational and rotational states that are quantized. Transitions between the lower-energy rotational states give rise to lines and those between the higher vibrational states to vibrational bands accompanied by numerous rotational lines within each band. High-resolution spectroscopic data reveal thousands of monochromatic absorption lines in each of the absorption bands. However, in practice, radiation emitted is never monochromatic, but instead spectral lines of finite widths are observed. Michelson (1895) initiated the theory of line broadening based on strong encounters in the sense of kinetic theory. This broadening of the spectral lines is due to: (1) natural causes (loss of energy in emission), (2) pressure broadening occurring due to molecular collisions, and (3) Doppler effect resulting from the difference in thermal velocities of

atoms and molecules. In the upper atmosphere, the Doppler broadening prevails in combination with pressure broadening, while the latter dominates in the lower atmosphere. For the larger pressures typical of the lower atmosphere, the most important line-broadening mechanism is pressure broadening (e.g., Goody, 1964), and the variation of the spectral absorption coefficient is expressed by the Lorentz profile. The spread of the line absorption with frequency is determined by the line-shape factor, which depends upon assumptions regarding the mode of broadening. Laboratory measurements of total band and line absorption, complemented by theoretical models of the strengths of molecular transitions, have enabled the creation of a large spectroscopic database (Rothman *et al.*, 1987) that is constantly being refined and improved.

It is possible to model the longwave radiative fluxes in the atmosphere by directly evaluating the contribution of the individual lines of atmospheric absorption bands. The earliest attempts to derive the infrared radiation fluxes in the atmosphere are discussed in the monograph by Elsasser (1942), who developed a simple graphical integration method to derive the total absorption coefficient at a given frequency. He assumed that each individual spectral line has a Lorentz shape and that the total absorption coefficient at a given frequency can be represented by the sum of absorption coefficients from an infinite series of equally spaced lines. Elsasser can also be credited with introducing the pressure dependence of the absorption coefficient for inhomogeneous atmospheric paths by appropriately scaling the optical mass. The inherent assumptions in Elsasser's pressure-scaling method were considered inadequate in a later study by Kaplan (1959). He described a more accurate method for the calculation of infrared fluxes and flux divergence by properly accounting for the temperature dependence of the absorption coefficient, and by applying the now-famous Curtis–Godson approximation (Goody, 1964) for the treatment of the inhomogeneous paths.

Although detailed spectroscopic information on line widths and intensities were available, early attempts at deriving the theoretical spectra without any kind of approximations were hampered by the non-availability of sufficient computing power and data-storage capabilities. With the advent of digital computers, methods that directly integrated the line spectra gained popularity. The first such attempt was made by Hitschfeld and Houghton (1961), who integrated the flux equation directly for the 9.6  $\mu\text{m}$  ozone band between 9.5 and 32.5 km. They did not use a spectral model and their treatment of the pressure effects was exact. A similar study by Drayson (1967) for the 15  $\mu\text{m}$   $\text{CO}_2$  band extended the approach to include non-homogeneous atmospheric paths by performing analytical integration over pressure. Use of the exact line-by-line techniques became more widespread with the availability of documented spectral-line data (McClatchey *et al.*, 1973) and the advent of high-speed digital computers.

However, the enormous number of spectral lines and the complexity of the inhomogeneous atmosphere still demanded copious amounts of computer time and resources and precluded such a task being undertaken for climate-model applications. However, they have been used as benchmark references for other simpler models (as discussed in the next subsection). The approximate approaches for treating absorption over finite spectral intervals involve band models. An illustration of how spectroscopic information is incorporated into the formulation of a band model along with a discussion of different types of models has been given by Cess and Tiwari (1972). Several different band models have also been discussed by Goody (1964), and applications to flux calculations have been numerous. Kiehl and Ramanathan (1983) compared the results of various band-model parameterizations to measurements and showed that the calculated and measured frequency-integrated absorptions agreed to within the experimental accuracy of 5 to 10%.

The inclusion of the quantum-mechanical details also proved to be important. For example it was shown (Augustsson and Ramanathan, 1977) that tens of weak isotopic and hot bands of CO<sub>2</sub> in the 8 to 20 μm region played a dominant role in the greenhouse effect for CO<sub>2</sub> concentrations exceeding present-day values by factor of 10 or larger (values that are considered to be reasonable for Earth's Archean atmosphere of two to four billion years ago), see Chapter 13.

In summary, with the state-of-the-art spectroscopy, the complexity of modeling the absorption and emission in the atmosphere of gases consisting of thousands of spectral lines has ceased to be a source of uncertainty. However, the same is not true for the far wings of distant spectral lines where the so-called “continuum absorption” prevails. More discussion on this appears in the following section.

### **5.2.3 *Radiation modeling***

The radiation-flux calculation algorithms used in earlier climate-sensitivity experiments were simple and represented an approximation to the exact solutions of the radiative-transfer equation. The models differed appreciably from each other. However the availability of better spectroscopic data contributed to the development of detailed radiation models that could generate the vertical distribution of fluxes in the atmosphere. These model simulations far exceeded our ability to make such observations. As a result, radiation models used in climate studies were developed in isolation. Symptomatic of this process is the treatment of clouds as flat plates with no inhomogeneities. Differences in model approaches together with an insufficient knowledge of the distribution of the radiatively active species in the atmosphere (water vapor, clouds, and aerosols) caused significant differences between the results of these models.

The perception of possibly significant uncertainties in the simulation of fundamental radiative processes affecting the proposed climate-change mechanisms, led the World Climate Research Program (WCRP) to sponsor an international effort called the Intercomparison of Radiation Codes in Climate Models (ICRCCM) with the goal of evaluating and improving solar and longwave radiative computations in climate models (Luther *et al.*, 1988). The ICRCCM made extensive use of the most detailed models and performed explicit integration over each of the tens of thousands of spectral lines in the thermal region of the spectrum. Figure 5.1 shows an example of the radiance spectrum measured by a High-resolution Interferometer Sounder (HIS) radiometer flying at 20 km altitude (Revercomb *et al.*, 1988). The curve clearly highlights the important spectral regimes for absorption by H<sub>2</sub>O, CO<sub>2</sub>, and O<sub>3</sub>.

While the spectra from these detailed models are believed to be accurate to better than 1%, uncertainties still remain due to the background absorption in the far wings of distant spectral lines and especially in the “continuum” region of the atmospheric window between 8 and 12  $\mu\text{m}$ . The cumulative effect of strong distant lines, although not important for gases like CO<sub>2</sub>, are critical for water vapor, especially in regions of weak absorption. One of the conclusions of the ICRCCM study was that in the absence of a widely accepted theory, the H<sub>2</sub>O continuum absorption masked the observed differences among the simpler models. The continuum absorption, which varies as the square of the water-vapor density, is an important mode of cooling in the lower troposphere (Roberts *et al.*, 1976). The most widely followed continuum formulation (Roberts *et al.*, 1976) ascribes most of the continuum absorption to the *e*-type (i.e., dependent solely on the water-vapor partial pressure). However, Clough and his collaborators (Clough *et al.*, 1989; Clough *et al.*, 1992) concluded, based on theoretical models of line shape and careful examination of the experimental data of Burch, that continuum is important at all frequencies. The *p*-type contribution (foreign-broadening) to the continuum caused the largest differences with Robert’s formulation at 200 mb in the troposphere (Clough *et al.*, 1992). Incidentally, this latter study also brought into focus the prominence of the far-infrared region of the longwave beyond 15  $\mu\text{m}$ . This far infrared consists of the pure rotation bands of H<sub>2</sub>O, the dominant mechanism for radiative cooling to space in the mid to upper troposphere (altitudes with pressure levels less than about 500 mb).

Another important outcome of the ICRCCM exercise was the call for an organized effort simultaneously to measure the spectral radiance along with the information on the atmospheric state, which, in early 1990s, culminated in the DOE-sponsored Atmospheric Radiation Measurement project at the Southern Grid Plains site in Oklahoma. The measured radiance spectra display (Figure 5.1) as much spectral detail as those produced from the line-by-line models themselves.

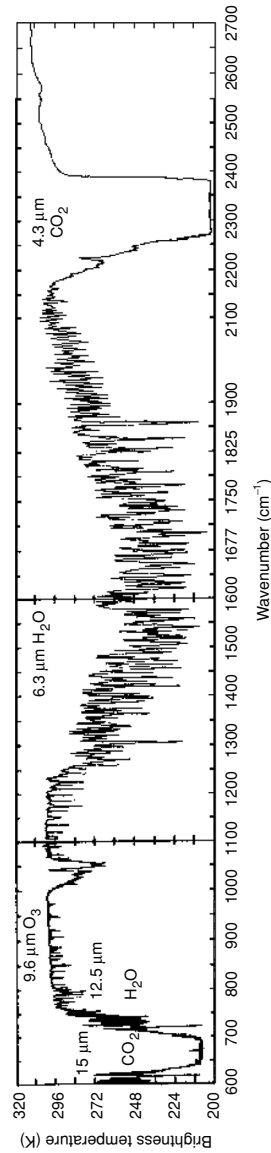


Figure 5.1. An example of a typical Earth-emitted radiance spectrum measured by the HIS radiometer (see text).

### 5.2.4 Beginning of the satellite era

With the advent of the satellite era in the early 1960s, it was possible to measure the radiation budget at the top of the atmosphere. Radiation-budget instruments measure the outgoing longwave radiation (OLR), incoming solar radiation, and reflected solar radiation. It required nearly two decades of evolution of satellite instrumentation before we could obtain a comprehensive database of radiative energy budget at the top of the atmosphere (Barkstrom, 1984). With the launch of the scanning radiometer as part of ERBE aboard the NOAA satellites, it was possible for the first time to get an observational assessment of the atmospheric greenhouse effect (Raval and Ramanathan, 1989), and cloud-radiative forcing (Ramanathan *et al.*, 1989; Harrison *et al.*, 1990). Another advantage provided by the scanning ERBE instrument was a simultaneous twin view of the Earth (paraphrasing Cess' oft-quoted description of ERBE): one with clouds and one without clouds. This approach provided the data needed to understand two fundamental issues in radiative forcing of climate: cloud forcing and atmospheric greenhouse effect.

## 5.3 Cloud-radiative forcing

Until the advent of satellite radiation-budget experiments, model studies were the main source of insights into the global radiative effects of clouds (Manabe and Wetherald, 1967; Schneider, 1972). These models suggested that clouds have a large net cooling effect on the planet. Satellite radiation budget instruments measure the OLR, incoming solar radiation, and reflected solar radiation. Numerous studies have attempted to estimate the net radiative effect of clouds with satellite radiation-budget data collected during the 1970s and early 1980s (see summary in Hartmann *et al.*, 1986). The accuracy of these studies with regards to the global and regional effects of clouds has been diminished by the limitation of the data available to define clear-sky and cloudy-sky radiation fields.

In the ERBE approach the TOA radiation budget can be written as:  $H = S(1 - A) - F$ ; where  $H$  is the net heating of the surface-atmosphere column,  $A$  is the albedo and  $F$  is the OLR to space. We can express  $A$  and  $F$  as the weighted sum of clear-sky value and overcast-sky value as follows:  $A = A_c(1 - f) + f A_o$  and  $F = F_c(1 - f) + f F_o$  where  $f$  is the cloud fraction and the subscripts  $c$  and  $o$  denote clear-sky and overcast-sky values. Substituting these definitions in  $H$ , we obtain Equation (5.1), where  $C_1$  and  $C_s$  are the longwave and shortwave cloud

$$H = \{S(1 - A_c) - F_c\} + C_1 + C_s \quad (5.1)$$

forcing and, as described below, are given by the difference in the radiation budget of the clear- and cloudy-sky values (Ramanathan *et al.*, 1989). In the present context,

the term “cloudy” refers to a mix of clear and overcast skies. Satellites mostly observe cloudy-sky values mixed with infrequent clear-sky values, and it takes great care and validated algorithms to infer clear-sky values. The clear-sky OLR also yields the atmospheric greenhouse effect, provided the longwave emission from the surface is known. These quantities are defined first.

*Greenhouse effect of the atmosphere ( $G_a$ )*. This follows the classical definition of the greenhouse effect, which is the effect of the atmosphere in reducing the longwave cooling to space. The term  $G_a$  is defined as  $G_a = E - F_c$  where  $F_c$  is the measured OLR for clear skies and  $E$  is the emission from the surface, which for a black body equals  $\sigma T_s^4$  with  $\sigma = 5.67 \cdot 10^{-8} \text{ W m}^{-2} \text{ K}^{-4}$  and  $T_s$  is the surface temperature.

*Longwave cloud forcing ( $C_1$ )*. Clouds reduce the OLR further and enhance the greenhouse effect. This enhancement of the greenhouse effect by clouds can be obtained by letting:  $C_1 = F_c - F$ , where  $F$  is OLR for average cloudy conditions (mixed clear and cloudy skies). In general,  $C_1$  is positive.

*Total greenhouse effect ( $G$ )*. The combined effect of cloud and the atmosphere on the greenhouse effect is:  $G = G_a + C_1 = E - F$ .

*Short wave cloud forcing ( $C_s$ )*. Clouds also enhance the albedo (reflectivity) of the planet, when compared with cloudless skies, thereby decreasing the planetary solar heating. This effect, referred as the cloud shortwave forcing,  $C_s$ , is estimated by differencing the solar energy absorbed by a cloudy region from that over just the clear-sky portion of that region, i.e.,  $C_s = S(1 - A) - S_c$ , where  $S$  is the solar insolation at TOA,  $A$  is the column albedo, and  $S_c$  is the clear-sky solar absorption;  $C_s$  is negative, indicating a cooling effect.

*Net cloud forcing ( $C$ )*. The net effect of clouds is given by the sum of the longwave and the shortwave cloud forcing, i.e.,  $C = C_1 + C_s$ . If  $C$  is negative, then clouds have a net cooling effect on the surface-atmosphere column.

With the above definitions, the radiation budget of the system can be expressed as in Equation (5.2):

$$H = \{S(1 - A_c) - E\} + G_a + C_1 + C_s \quad (5.2)$$

In summary, we have observable definitions for determining the effect of clouds and the atmosphere. The results here are based on the five-year scanner data collected by ERBE between 1985 and 1990.

### 5.3.1 Radiation budget of the twin Earth

The OLR for clear and cloudy skies is shown in Figure 5.2. Clear skies reveal a general decrease in emission from tropical to polar regions, except for the following important exceptions: the maximum OLR is in the dry sub-tropical

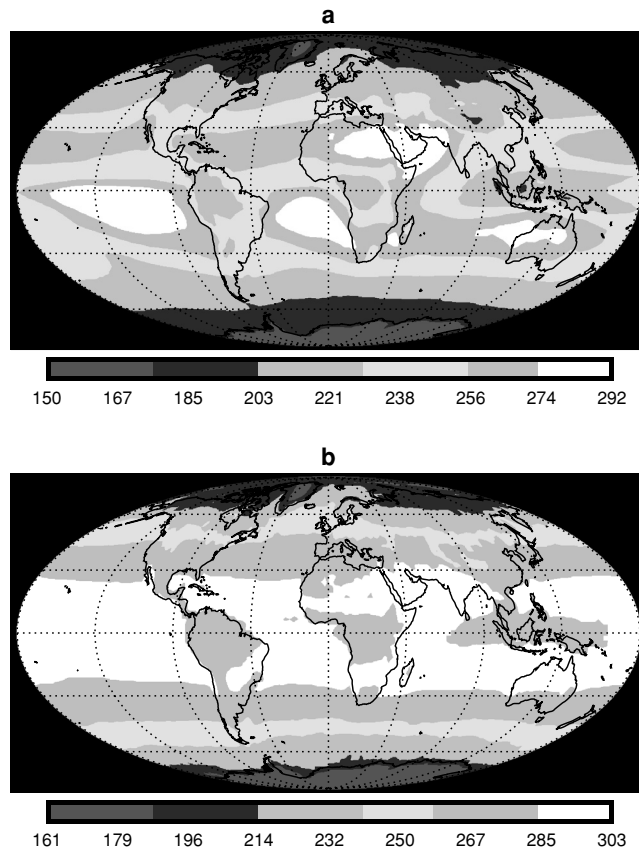


Figure 5.2. Earth Radiation Budget Experiment data averaged over 1985 to 1989 for (a) cloudy-sky (average of clear and cloudy skies) OLR and (b) clear-sky OLR (in  $\text{W m}^{-2}$ ).

subsidence regimes, a minimum in the humid inter-tropical convergence zone (ITCZ) and western Pacific warm-pool regions. As expected, cloudy skies reveal significant east–west and north–south variations. The difference between the cloudy-sky OLR (Figure 5.2a) and clear-sky fluxes (Figure 5.2b) is the longwave cloud forcing.

The albedos are shown in Figure 5.3. It is important to note that these are calibrated broad-band (0.3 to 4  $\mu\text{m}$ ) albedos (as opposed to the narrow band visible albedos from GOES or NOAA weather satellites). Darkest are the equatorial oceans and tropical forests; brightest are the deserts and snow-covered polar regions. With clouds, the regional differences practically disappear. It is intriguing to note that, with clouds, the very cloudy regions of the equatorial rain forests and the Indo-Pacific warm pool are just as bright as the nearly cloudless major desert regions in northern Africa, Australia, and others in the world.

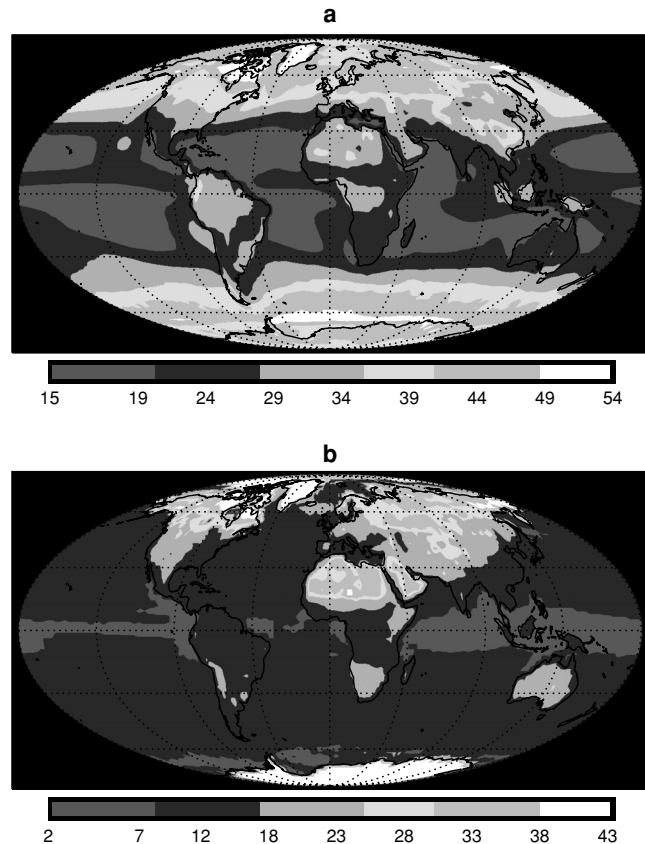


Figure 5.3. Earth Radiation Budget Experiment data (%) averaged over 1985 to 1989 for (a) cloudy-sky albedo (average of clear and overcast skies) and (b) clear-sky albedo.

### **5.3.2 Global cloud forcing: do clouds heat or cool the planet?**

The five-year global mean energy budgets for clear and cloudy regions are illustrated in Figure 5.4. Clouds reduce the absorbed solar radiation by  $48 \text{ W m}^{-2}$  ( $C_s = -48 \text{ W m}^{-2}$ ) while enhancing the greenhouse effect by  $30 \text{ W m}^{-2}$  ( $C_1 = 30 \text{ W m}^{-2}$ ), and therefore clouds cool the global surface–atmosphere system by  $18 \text{ W m}^{-2}$  ( $C = -18 \text{ W m}^{-2}$ ) on average. The mean value of  $C$  is several times the  $4 \text{ W m}^{-2}$  heating expected from doubling of CO<sub>2</sub> and thus Earth would probably be substantially warmer without clouds.

### **5.3.3 Regional cloud forcing: cloud systems with large forcing**

Five-year averages of the  $C_s$  (Figure 5.5a) and regional  $C_1$  (Figure 5.5b.) reveal the major climatic regimes and organized cloud systems of Earth. Maxima in  $C_1$  are

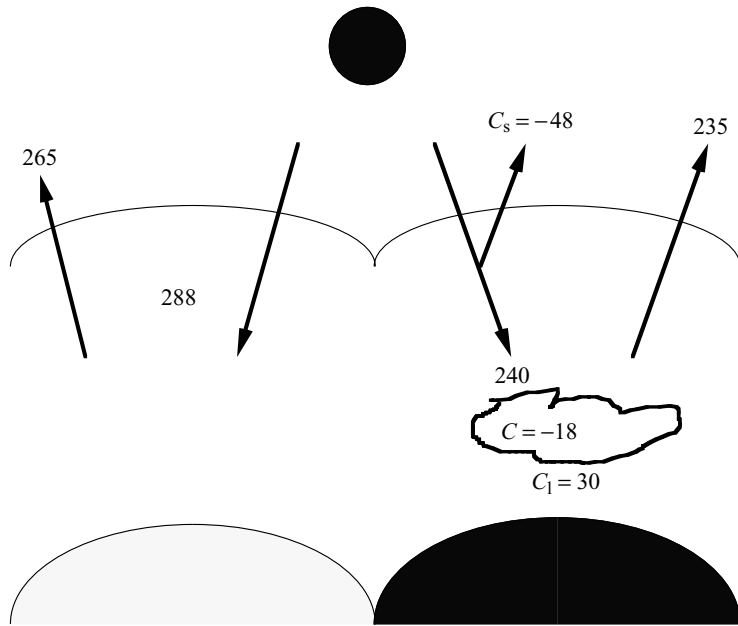


Figure 5.4. Global average clear-sky radiation budget (left panel) and cloud radiative forcing (right panel) from ERBE. The values ( $\text{W m}^{-2}$ ) are for five-year averages between 1985 and 1989. From Ramanathan *et al.*, 1989; Harrison *et al.*, 1990; Collins *et al.*, 1994.

found in regions of moderately thick ( $\geq 1 \text{ km}$ ) upper-troposphere cirrus clouds, such as deep convective regions in the tropics and jet-stream cirrus in mid and high latitudes. These clouds absorb longwave energy from the warmer regions below and re-radiate to space at the colder upper-troposphere temperature, thus leading to a large reduction in OLR. Maxima in  $C_s$  are found in regions of optically thick low-level clouds (stratus and marine strato-cumulus), precipitating cloud systems (extra-tropical cyclones) and deep convective-cirrus systems of the tropics (e.g., Ramanathan *et al.*, 1989; Harrison *et al.*, 1991).

- *Deep convective-cirrus systems.* Maxima in  $C_1$  of 60 to 100  $\text{W m}^{-2}$  found over the convectively disturbed regions of the tropics, including the tropical western Pacific, the eastern equatorial Indian Ocean, and the equatorial rain forest regions of South America and Africa. Seasonally (not shown here) the monsoon cloud systems and the ITCZ cloud systems exhibit comparably large values of  $C_1$ . The strong greenhouse heating by these upper-tropospheric cloud systems is accompanied by a correspondingly large cooling due to reflection of solar radiation.
- *Extra-tropical storm track cloud systems.* In addition to the convective and ITCZ tropical clouds, persistent bright clouds that reflect more than 75  $\text{W m}^{-2}$  of solar radiation ( $C_s < -75 \text{ W m}^{-2}$ ) are found polewards of about 35° in the Pacific, Atlantic, and the Indian

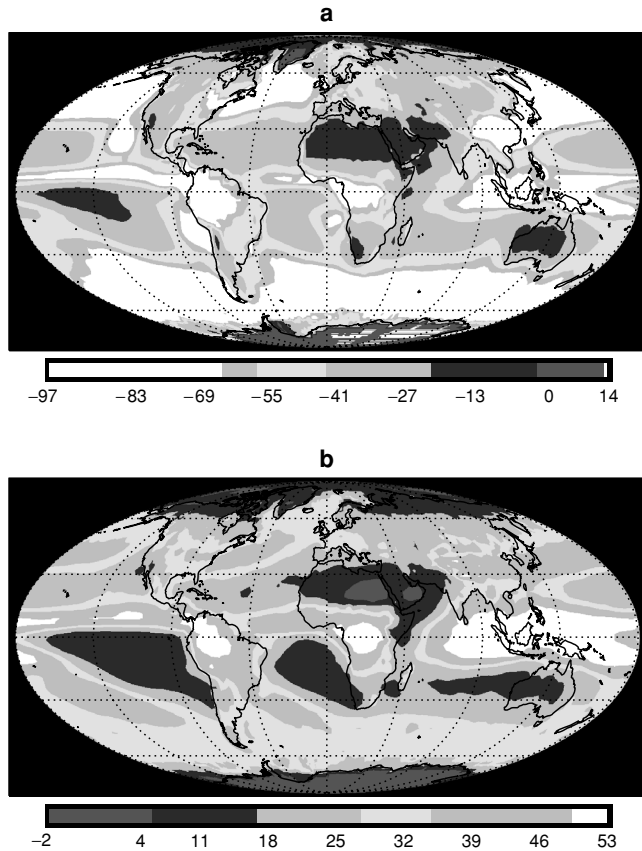


Figure 5.5. Shortwave (a) and longwave (b) cloud radiative forcing (in  $\text{W m}^{-2}$ ) from ERBE (1985–1989).

oceans. Cloud systems associated with extra-tropical cyclones and the stratus that follows the passage of these cyclones are responsible for this cooling.

- *Marine strato-cumulus coastal systems.* These sub-tropical cloud systems also contribute more than  $75 \text{ W m}^{-2}$  to  $C_s$  and extend as far as a thousand kilometers from the western coasts of North America, South America, and South Africa.

An intriguing feature of Figures 5.5 and 5.6 is that in tropical regions where the clouds significantly affected the longwave and shortwave fluxes (Figure 5.5), the longwave and shortwave cloud-forcing terms nearly cancel each other (Figure 5.6). This feature has defied an explanation so far (see Kiehl, 1994 for a partial resolution of this issue). *Does the near cancellation at the TOA imply a negligible role in tropical climate?*

Not necessarily, according to Stephens and Webster (1979) and Ramanathan (1987), who showed that these clouds alter significantly the vertical (between the

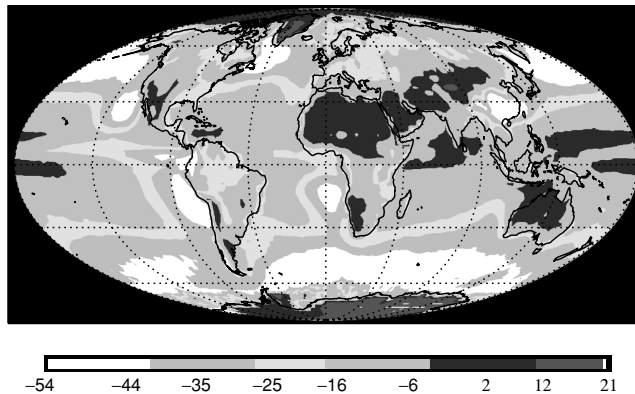


Figure 5.6. Net cloud radiative forcing ( $= C_s + C_1$ ), in  $\text{W m}^{-2}$  (ERBE, 1985–1989).

ocean and atmosphere) and horizontal (longitudinal and meridional) heating gradients in the ocean and the atmosphere. A significant fraction of the longwave cloud forcing converges into the troposphere, because the clouds reduce the OLR escaping to space, but, the back radiation from the base of these clouds are absorbed by the intervening moist tropical atmosphere. The negative shortwave forcing is mostly due to reduction of solar radiation to the sea surface; in other words, clouds, like a translucent mirror, shield the surface from solar radiation by reflecting it back to space.

#### 5.4 Atmospheric greenhouse effect: global and regional averages

Consider first a one-dimensional system with the surface emitting like a black body. The clear-sky outgoing longwave radiation ( $F_c$ ) and  $G_a$  are related by Equation (5.3), where  $T_s$  is the surface temperature, and  $G_a$ , by definition is given by

$$F_c = \sigma T_s^4 - G_a \quad (5.3)$$

Equation (5.4), where  $\tau_v$  represents the optical depth between TOA and  $z'$  and the

$$G_a = \int_{\infty}^{\infty} dz' \int_{4 \mu\text{m}}^{500 \mu\text{m}} [1 - e^{-\tau_v(z', \infty)}] \frac{dB_v(Z')}{dz'} dv \quad (5.4)$$

expression in square parentheses thus represents the absorptance. From Equation (5.4), we note that  $G_a$  is the reduction in the outgoing longwave radiation due to the presence of the atmosphere. From Equation (5.4), it is seen that the reduction in OLR depends on two factors:  $\tau_v$ , the optical depth; and the vertical temperature gradient (note:  $dB_v/dZ \equiv [dB_v/dT]^* [dT/dz]$ ). Without a radiatively active atmosphere, i.e.,  $\tau_v = 0$ ,  $G_a = 0.0$  and OLR would be identically equal to

$\sigma T_s^4$ . Likewise, without a vertical temperature gradient,  $dB_v/dz = 0$ , and  $G_a = 0$ . It is obvious  $G_a$  includes the contribution from the entire troposphere and the stratosphere with weight given to all regions. Unless otherwise mentioned the results summarized here are taken from Inamdar and Ramanathan (1998).

The greenhouse effect of the atmosphere and clouds ( $G$ ) is obtained from Equation (5.5), where  $F$  is the OLR for the average cloudy skies. Note that  $G = G_a + C_1$ ,

$$F = \sigma T_s^4 - G \quad (5.5)$$

where  $C_1$ , the longwave cloud forcing (Ramanathan *et al.*, 1989) denotes the enhancement of the greenhouse effect by clouds.

*Global-annual mean values.* The global-annual means for the surface temperature and the different radiative flux parameters extracted from ERBE are shown in Figure 5.7. The ERBE clear-sky classification scheme is known to be inefficient over the ice-covered surfaces. Hence, while Figure 5.7a shows the results for the entire planet, Figure 5.7b shows results for the ice-free regions. The ice-covered portion of Earth constitutes approximately 6% of the globe. It is apparent from Figure 5.7b that the global surface temperatures have a warmer bias of about 4 K due to the exclusion of ice surfaces. Other uncertainties in the data are discussed in Inamdar and Ramanathan (1998).

The global average  $G_a$  is  $131 \text{ W m}^{-2}$  or the normalized  $g_a$  is 0.33, i.e., the atmosphere reduces the energy escaping to space by  $131 \text{ W m}^{-2}$  (or by a factor of 1/3). The ocean regions have a slightly larger greenhouse effect (0.35 for ocean vs. 0.33 for land) compared with the land (Figure 5.7b). In order to get another perspective on the results shown in Figure 5.7, we note that a doubling of  $\text{CO}_2$  (holding the surface and atmospheric temperature fixed) will enhance  $G_a$  by about  $4 \text{ W m}^{-2}$ . We should note that the  $g_a$  shown in Figure 5.7 includes the greenhouse effect of water vapor and all other greenhouse gases including  $\text{CO}_2$ ,  $\text{O}_3$ , and several trace gases.

*Regional values.* The regional distribution of the annual mean greenhouse effect and column water vapor is shown in Figure 5.8. Figure 5.8a shows the normalized greenhouse effect,  $g_a = G_a/\sigma T_s^4$ . A large fraction of the spatial variation in  $G_a$  is due to the variations in  $T_s$ . The contributions from variations in  $T_s$  are essentially removed in the normalized greenhouse effect ( $g_a$ ), such that regional variations of  $g_a$  (shown in Figure 5.8a) reveal the effects of variations in atmospheric humidity and lapse rates. As shown in Figure 5.8,  $g_a$  increases from pole to equator largely due to the corresponding increase in humidity (shown in Figure 5.8b; also see Raval and Ramanathan 1989 and Stephens and Greenwald, 1991). Furthermore, for the same latitude zone, the continental  $g_a$  values are significantly lower than the ocean values indicating that the land regions are drier than the oceanic regions.

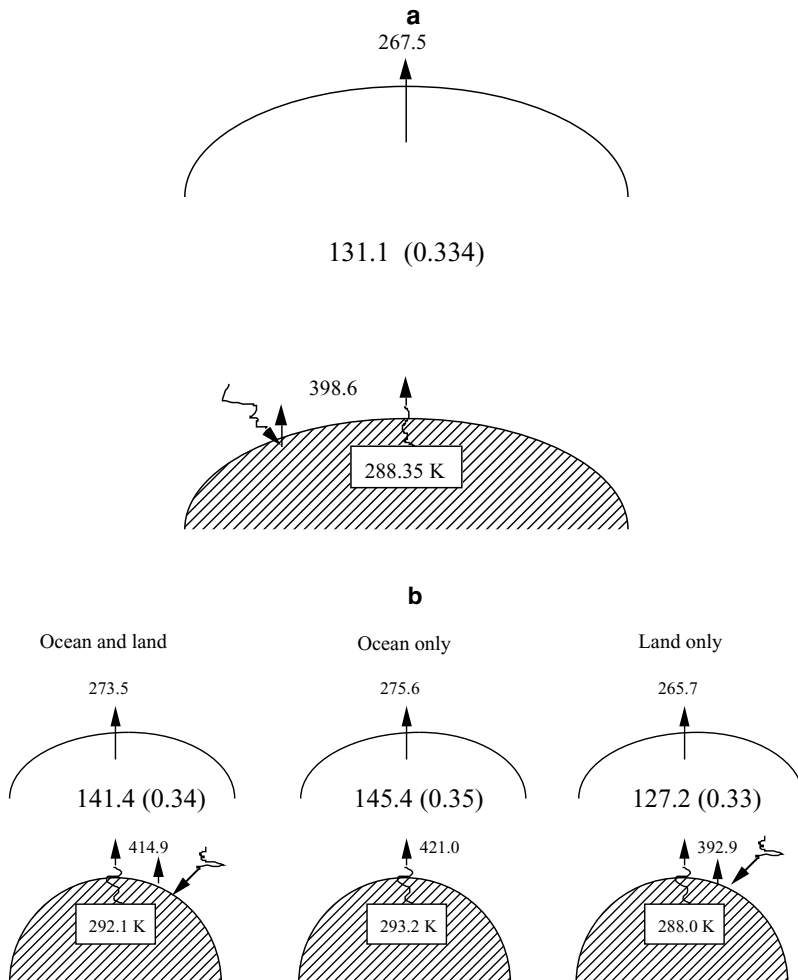


Figure 5.7. (a) Global average of surface temperature, surface emission, outgoing longwave radiation (OLR), and atmospheric greenhouse effect derived from ERBE, GEOS data (1985–89) and Salisbury and D'Aria (1992) surface emissivity tables. The results include all regions of the globe including sea ice and permanent ice. Uncertainties: surface emission,  $\pm 3 \text{ W m}^{-2}$ ; TOA flux,  $\pm 5 \text{ W m}^{-2}$ ; GA,  $\pm 6 \text{ W m}^{-2}$ . (b) Global average of surface temperature, surface emission, outgoing longwave radiation, and atmospheric greenhouse effect derived from ERBE, NMC-blended sea-surface temperature (SST) (for the oceans), NMC station surface temperatures (for the land), and surface emissivities based on Salisbury and D'Aria (1992) vegetation-index tables, for the period 1988–89. Results exclude ice-covered regions (*c.* 6% of Earth's surface). Uncertainties: surface emission,  $\pm 3 \text{ W m}^{-2}$ ; TOA flux,  $\pm 5 \text{ W m}^{-2}$ ; GA,  $\pm 5 \text{ W m}^{-2}$ .

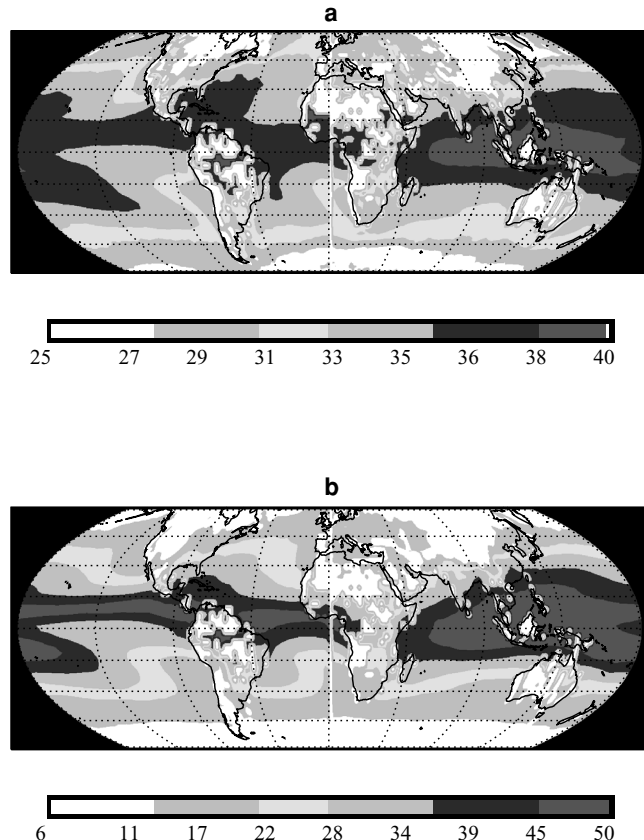


Figure 5.8. (a) Regional distribution of the annual mean atmospheric greenhouse effect ( $g_a$ ) from 1988 and 1989 data (%). (b) Regional distribution of the annual mean total precipitable water  $w$  from 1988 and 1989 NVAP (NASA water vapor project) data ( $\text{kg m}^{-2}$ ).

As shown by Raval and Ramanathan (1989) and Stephens (1990), geographical variations in  $g_a$  are dominated by the dependence of  $g_a$  on water vapor ( $w$ ) and  $T_s$ , i.e.,  $g_a$  increases with  $w$  which in turn increases with  $T_s$ . The equator-to-pole decrease in  $g_a$  is largely due to the corresponding decrease in  $T_s$  and  $w$ .

The atmospheric dynamics also has a strong influence on  $g_a$ . We can distinctly see enhanced values of  $g_a$  (top panel) and  $w$  (bottom panel) in the deep convective regions of the western Pacific and the ITCZ, surrounded by lower values of  $g_a$  in the sub-tropical high-pressure belt with strong subsidence. The subsidence over the desert regimes of North Africa (Sahel desert), South Africa (Kalahari desert), Asia (Gobi desert), South America, and Australia are also quite marked with lower values of  $g_a$ . These regions are characterized by very low surface emissivities (significantly below 1) and low precipitable water amounts (Figure 5.8b) causing

an anomalously low greenhouse effect. In summary Figure 5.8 reveals a remarkable consistency between regional variations in  $g_a$  and  $w$ , which suggests that variations in water vapor rather than lapse rates contribute to regional variations in  $g_a$ .

### 5.5 Understanding water-vapor feedback using radiation budget data: an example

The response of water vapor and its greenhouse effect (i.e.,  $g_a$ ) to surface and atmospheric temperature changes is a fundamental issue in climate dynamics. Since water-vapor distribution is determined by both thermodynamics and dynamics, this response can depend on the spatial scales and the time scales of the temperature variations. Ideally we need data that can be integrated over spatial scales large enough to average over several dynamical processes such as the ascending and descending branches of the tropical circulation (Soden, 1997). With respect to time scales we need a spectrum of scales ranging from seasonal to decadal scales to examine the dependency on time scales. Such long-term datasets are not yet available. However with the five-year ERBE dataset we can examine the annual time scales over the entire tropics and the planet. In particular, as shown by Inamdar and Ramanathan (1998), water-vapor distribution,  $g_a$ , and  $T_s$  undergo large seasonal variations even when averaged over the entire tropics or the globe. Before summarizing the results, we will clarify an oft-held misconception that only the lower layers of the troposphere contribute to  $G_a$ .

Figure 5.9 shows the sensitivity parameters  $dF_c/d(\ln w)$  and  $dG_a/d(\ln w)$  as a function of altitude. In each layer of the atmosphere, we change the water-vapor concentration by 1% and estimate the change in OLR and  $G_a$ . The figure clearly demonstrates that both  $G_a$  and OLR (i.e.,  $F_c$ ) receive comparable contribution from all layers of the troposphere. We next give the following background to aid the interpretation of the results presented later.

The fundamental longwave climate-feedback parameter is  $dF/dT_s$ , and from Equation (5.3), Equation (5.6) is obtained.

$$dF/dT_s = 4\sigma T_s^3 - dG/dT_s = 4\sigma T_s^3 - (dG_a/dT_s + dC_1/dT_s) \quad (5.6)$$

The water-vapor feedback effect is contained in  $dG_a/dT_s$ ; the cloud feedback effect is contained in  $dC_1/dT_s$  and lapse-rate changes will influence both  $dG_a/dT_s$  and  $dC_1/dT_s$ . Considering first  $dG_a/dT_s$ , we obtain Equation (5.7) from Equation (5.3). For a uniform change in surface

$$dG_a/dT_s = 4\sigma T_s^3 - dF_c/dT_s \quad (5.7)$$

and atmospheric temperature (i.e., without lapse-rate feedback) and without any change in water-vapor amount (i.e., no water-vapor feedback),  $dF_c/dT_s =$

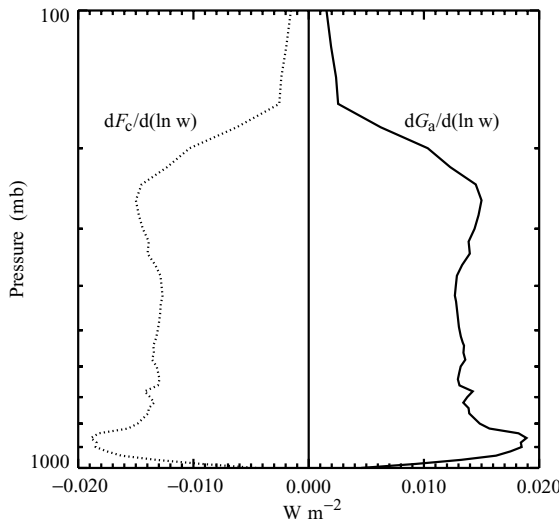


Figure 5.9. Sensitivity of OLR and  $G_a$  to height-dependent perturbations in water-vapor mixing ratio. Sensitivity (per unit % change in  $w$ ) has been derived by averaging the sensitivity over a range of RH perturbations between  $-20$  to  $20\%$  from the standard tropical profile.

$3.3 \text{ W m}^{-2} \text{ K}^{-1}$  (Ramanathan *et al.*, 1981). Thus for lapse rate or water vapor to exert a positive feedback, requires  $dF_c/dT_s < 3.3$  for positive feedback;  $\approx 3.3$  for no feedback;  $\geq 3.3 \text{ W m}^{-2} \text{ K}^{-1}$  for negative feedback.

Radiative-convective models with fixed relative humidity assumption yield (e.g., see Ramanathan *et al.*, 1981)  $dF_c/dT_s \approx 2 \text{ W m}^{-2} \text{ K}^{-1}$ .

To rephrase the above criteria in terms of Equation (5.7), we note that for the global average  $T_s = 289 \text{ K}$ ,  $4\sigma T_s^3 = 5.47 \text{ W m}^{-2} \text{ K}^{-1}$  and we obtain from Equation (5.7)  $dG_a/dT_s > 2.2$  for positive feedback;  $\approx 2.2$  for no feedback;  $< 2.2 \text{ W m}^{-2} \text{ K}^{-1}$  for negative feedback.

The observed annual cycles of  $T_s$ ,  $g_a$ , and precipitable water ( $w$ ) are shown respectively in Figure 5.10a,b, and c for the entire tropics ( $30^\circ \text{N}$ – $30^\circ \text{S}$ ); in Figures 5.11a–c for the globe ( $90^\circ \text{N}$ – $90^\circ \text{S}$ ). The precipitable water,  $w$ , is resolved into three tropospheric layers:  $w_1$  for lower (surface–700 mb),  $w_2$  for middle (700–500 mb) and  $w_3$  for upper (500–300 mb) troposphere.

For the tropics,  $T_s$  peaks in March/April, while for  $90^\circ \text{N}$ – $90^\circ \text{S}$ ,  $T_s$  peaks in July. We can qualitatively interpret the phase of the annual cycle as follows. The tropical annual cycle is dominated by the coupled ocean–atmosphere system and as a result, the temperature response lags behind the forcing by a maximum of about three months ( $\pi/2$ ); thus, with the solar insolation peaking in December 21, the temperature peaks in late March as shown in Figure 10. In addition to the annual

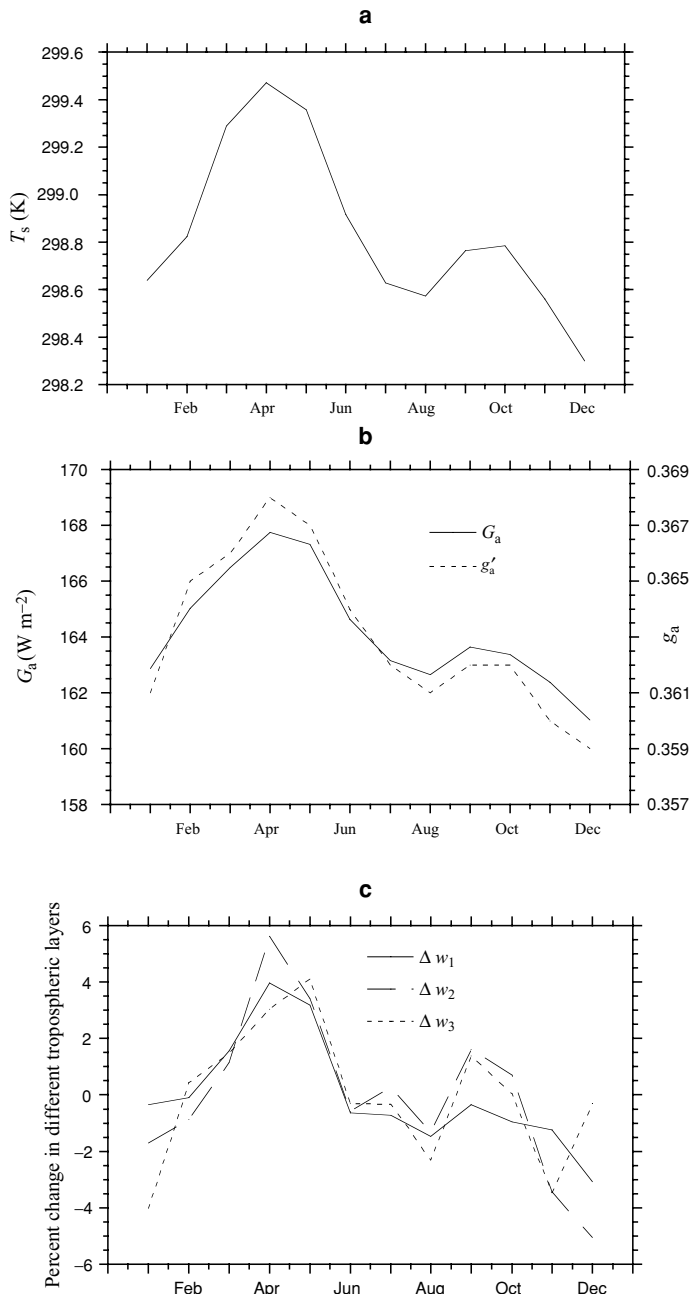


Figure 5.10. Annual cycles for the tropics ( $30^\circ \text{N}$ – $30^\circ \text{S}$ ). (a) surface temperature ( $T_s$ ) obtained from the same sources as in Figure 5.7; (b) atmospheric greenhouse effect ( $G_a$ ) and the normalized atmospheric greenhouse effect  $g_a$  shown by dashed line; and (c) percent change in precipitable water in three tropospheric layers, namely lower ( $w_1$  between surface and 700 mbar), middle ( $w_2$  between 700 and 500 mbar), and upper ( $w_3$  between 500 and 300 mbar).

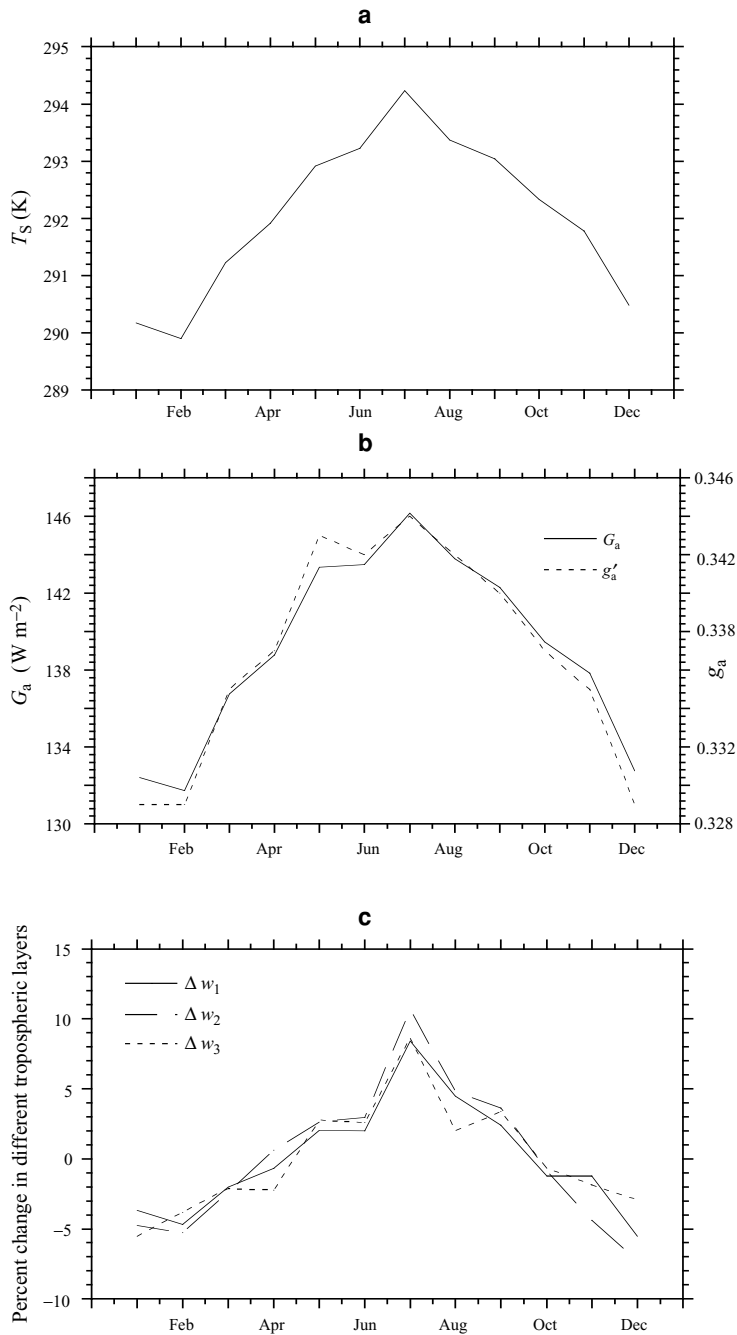


Figure 5.11. Same as Figure 5.10, but for 90° N–90° S.

cycle, the figure also reveals a semi-annual cycle, whose amplitude is comparable to the annual-cycle amplitude.

The extra-tropical and global annual cycle is most likely dominated by the hemispherical asymmetry in the land fraction. During the northern-hemisphere summer (June, July, and August), the large land masses warm rapidly (with about a one-month lag) which dominates the hemispherical and global mean response; however, during the southern-hemisphere summer, the relatively smaller fraction of land prevents a corresponding response. Thus, the globe is warmest during June/July and is coldest during December/January.

Both Figures 5.10 and 5.11 reveal that  $g_a$ ,  $w_1$ ,  $w_2$ ,  $w_3$ , and  $T_s$  are positively correlated. The figures again reveal the consistency between the radiation-budget data and the water-vapor data. When  $w$  and  $g_a$  are correlated with  $T_s$ , the best correlation coefficient is obtained for a phase lag of less than a month (as shown later). This near-zero phase lag rules out the possibility of variations in  $g_a$  or  $w$  driving variations in  $T_s$ ; were this to be the case,  $T_s$  should lag behind the forcing by at least more than a month. On the other hand, since convective time scales are less than a month, it is reasonable to expect that variations in  $g_a$  and  $w$  are driven by variations in  $T_s$  without much phase lag. The deduction is that the correlation coefficient between  $g_a$  and  $T_s$  or that between  $w$  and  $T_s$  is the feedback parameter, valid at least for annual time scales.

Scatter plots of  $G_a$  versus  $T_s$  for the tropics ( $30^\circ$  N– $30^\circ$  S) and globe ( $90^\circ$  N– $90^\circ$  S) are shown in Figure 5.12, and similar plots of  $F_c$  versus  $T_s$  are shown in Figure 5.13. The feedback term  $dG_a/dT_s$  derived from the annual cycle of monthly mean values are summarized in Figure 5.14 (ocean and land). The  $G_a - T_s$  correlation was performed by successively including larger domains extending in increments of five degrees on either side of the equator (e.g.,  $5^\circ$  N– $5^\circ$  S,  $10^\circ$  N– $10^\circ$  S, and so on). The period 1985–87 was marked by ENSO, which peaked with the El-Niño event in 1987. Since the annual-cycle signals were weak during this ENSO, we employ only the years 1988–89 for the correlation analysis here. The thick solid line depicted in Figure 5.14 has been derived using the annual cycle from station data, while the dashed line is derived employing the GEOS surface-temperature data.

Focusing first on the clear-sky sensitivity values (as opposed to the all-sky values shown by solid circles), we infer the following features from Figure 5.14.

- Between  $10^\circ$  N and  $10^\circ$  S (not shown),  $dG_a/dT_s$  ( $7\text{--}10 \text{ W m}^{-2} \text{ K}^{-1}$ ) exceeds the black-body-emission value of about  $6 \text{ W m}^{-2} \text{ K}^{-1}$ , thus reproducing the so-called super greenhouse effect inferred from latitudinal variations in  $G_a$  and  $T_s$  (Raval and Ramanathan, 1989) and from El-Niño-induced variations (Ramanathan and Collins, 1991). The large value of  $dG_a/dT_s$  is due to the increase in frequency of convection with  $T_s$  (Waliser *et al.*,

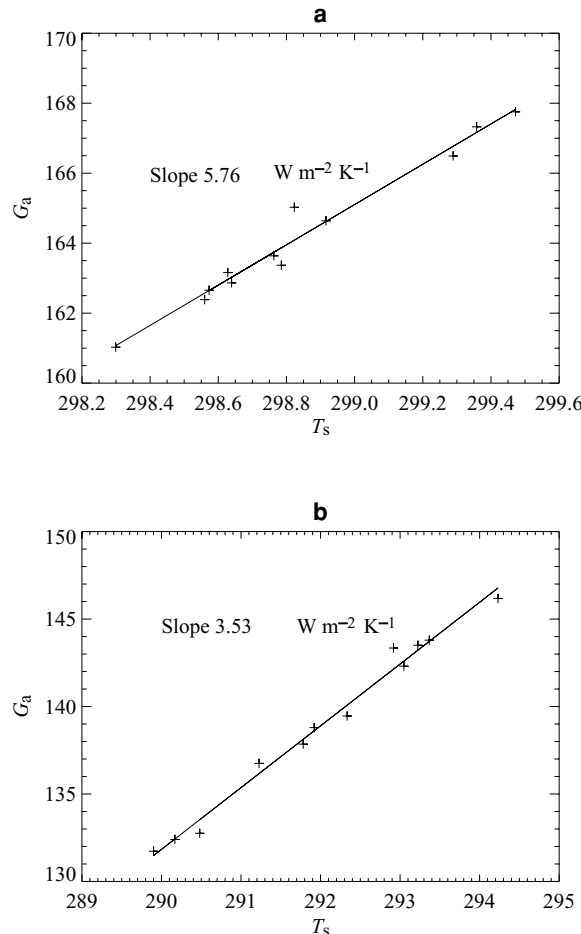


Figure 5.12. Scatterplots of  $G_a$  versus  $T_s$  using the annual cycles shown in Figures 5.10 and 5.11 for the two domains (i.e., 30°N–30°S and globe). The slope  $dG_a/dT_s$ , representing the water-vapor feedback sensitivity parameter, obtained from the least square fit of the data, is inset in the figures.

1993) and the subsequent increase in mid and upper tropospheric water vapor (Hallberg and Inamdar, 1993). We have to bear in mind, however, that both temperature effect (as represented by the Planck and lapse-rate feedbacks) and moisture feedbacks contribute to the observed  $dG_a/dT_s$ , as can be inferred from Equation (5.4); see also Inamdar and Ramanathan, 1994.

- Away from the equatorial regions,  $dG_a/dT_s$  decreases rapidly and asymptotes to the global mean value of about 3.5  $\text{W m}^{-2} \text{K}^{-1}$ . The enhanced trapping in the equatorial regions is compensated by enhanced emission to space from the sub-tropics and the extra-tropics. The enhanced emission in the sub-tropics is most likely due to the drying effect of deep convection (as evidenced from the all-sky flux changes discussed later); in the

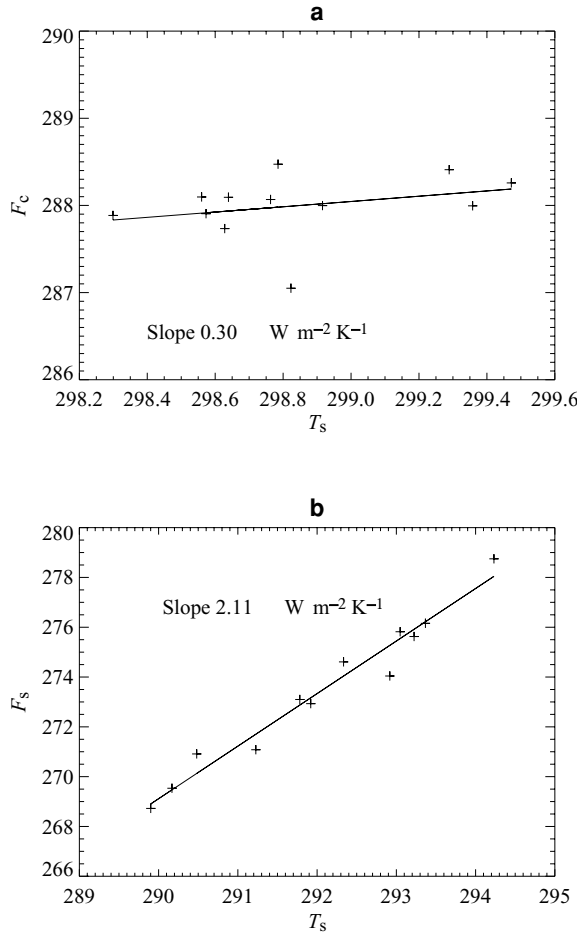


Figure 5.13. Same as in Figure 5.12 but for  $F_c$  versus  $T_s$ .

extra-tropics, on the other hand, temperature changes are confined largely to the northern-hemisphere land regions, which are not as effective as oceanic regions in enhancing water vapor in the atmosphere (this point is discussed in detail later). The magnitude of the feedback, as well as the corresponding variation in water vapor is consistent with values we expect for the fixed relative-humidity models, as is indeed seen by comparing the model values shown in Figure 5.14.

- Upon comparing with the all-sky values, we see that the cloud longwave forcing feedback term does not contribute to the global sensitivity. This does not, however, imply that clouds do not change. In fact, in the equatorial regions, the all-sky sensitivity is much larger thus indicating a large increase in convective clouds. In the sub-tropical regions, however, the drying effect of increased equatorial convection decreases the sensitivity to very close to clear-sky values.

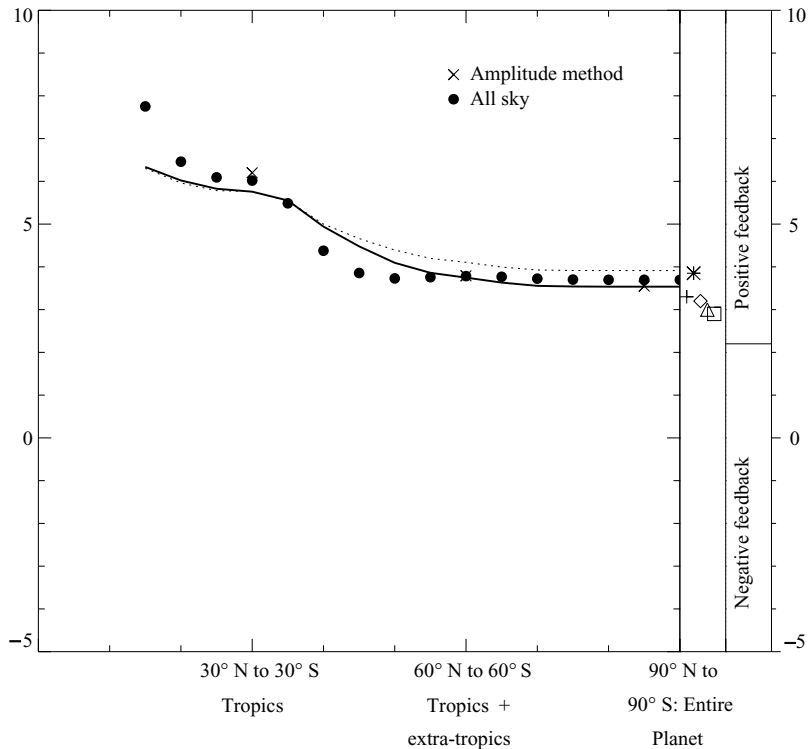


Figure 5.14. Feedback sensitivity parameter  $dG_a/dT_s$  for different latitude ranges (ocean plus land). The solid line depicts results, which use the data for the land-surface temperatures (1988–1989), while the dashed line employs the GEOS data. The results derived from the amplitude method ( $\times$ , see text), and also the ERBE all-sky OLRs ( $\bullet$ ) are shown in the second right box, while the box at the extreme right marks the range of  $dG_a/dT_s$  into regions of positive and negative feedback. Other data points are as follows:  $\square$ , Arrhenius (1896);  $*$ , Manabe and Wetherald (1967);  $\diamond$ , Mitchell, results reported in Cess *et al.*, 1989;  $+$  Raval and Ramanathan (1989);  $\triangle$  Cess *et al.* GCM intercomparison study (1989).

The data, however, reveal the sub-tropical drying effect of deep convection, qualitatively similar to that suggested by Lindzen (1990); but unlike Lindzen's mechanism, the drying effect is not sufficiently large and the positive water-vapor feedback dominates in the tropics. One possible reason is the failure of Lindzen's mechanism to account for the large super greenhouse effect in the low latitudes and the advection of moisture from the moist-convective regions to the dry subsidence regions.

However, our results do not necessarily confirm the positive feedback resulting from the fixed relative humidity models for global warming, for the present results are based on annual cycle. We need additional tests with decadal time-scale data for a rigorous test. Nevertheless, the analysis confirms that water vapor has a positive

feedback effect for global-scale changes on seasonal to inter-annual time scales. In addition, the results presented here provide a starting point for validating general circulation models.

## 5.6 Discussion: where do we go from here?

The results presented here clearly demonstrate that radiation-budget data, when integrated with correlative climate data, can provide valuable insights into the physics and dynamics of climate feedback and forcing. We restrict our comments that are germane to the topic of this paper, i.e., radiative forcing and feedback. First, we need improvements in data on several fronts.

### 5.6.1 Needed improvements in observations

*Radiation budget data.* We need to reduce the uncertainty in the retrieval of fluxes (needed for climate studies) from the radiances measured by satellites. These uncertainties can be of the order of  $50 \text{ W m}^{-2}$  for instantaneous values and about  $5 \text{ W m}^{-2}$  for time and spatial mean values. In addition, we need to improve the identification of clear-sky values from the cloudy pixels. Both these issues require high-resolution (few kilometers or less) cloud data. The recently launched CERES radiation-budget instrument onboard the TRMM (Tropical Rainfall Mapping Mission) and Terra (a NASA-EOS satellite) has such capabilities, and higher quality data are expected soon. Furthermore, all of the currently available radiation-budget data have severe diurnal sampling bias (sampling the planet at one or two local times each day). We need to launch the instruments on geostationary satellites to cover all times of day for the entire planet.

*Cloud cover and properties.* Recall that the cloud forcing approach avoids entirely the need for cloud-fraction information. While this is a strength of the approach and enabled us to make progress, we need the cloud data to make further progress towards a physical understanding of how clouds influence the radiative forcing of the planet. The newly launched MODIS instrument on Terra will yield higher quality data on cloud optical depths and cloud fraction. However, much progress in instrumental capability is needed in this area.

*Vertical structure of water vapor and its greenhouse effect.* A central issue in the water-vapor feedback problem has been the role of vertical structure of variability in the water-vapor distribution and the associated sensitivity of climate. One of the greatest uncertainties in the feedback issue, according to the IPCC (1995) document, is that related to the redistribution of water vapor. Divergent views prevail on the variability of tropospheric humidity, thus masking the actual sensitivity of the water-vapor greenhouse effect to height-dependent changes in the concentration

of water vapor. The latter may also represent uncertainties in the measurement of tropospheric humidity, especially in the upper troposphere. Lindzen (1990) argued in favor of enhanced climate sensitivity to the upper-tropospheric humidity to advocate his drying hypothesis. He suggested that it is the upper-tropospheric humidity that is the most important and stressed the need to evaluate the sensitivity of the radiative budget of the atmosphere to height-dependent changes of moisture. The study by Shine and Sinha (1991), however, suggested that the atmospheric response to increased concentrations of greenhouse gases is closer to a constant relative change at all altitudes thus translating into a larger absolute change in the lower troposphere. Hence the peak response is obtained in the lower troposphere ( $\sim 850$  mb) due to the continuum absorption. Spencer and Braswell (1997) concluded that fluctuations in the clear-sky outgoing longwave flux are most sensitive to the upper tropical free troposphere where the sensitivity is greatest at the lowest humidities. A recent study (Schneider *et al.*, 1999) suggested that the largest contribution to the sensitivity is from layers between 450 and 750 mb, while the smallest contribution is from layers above 230 mb.

These apparently glaring differences can be traced to a consideration of different structures for the variability of the tropospheric water vapor. Part of the reason for the uncertainty has been the non-availability of reliable measurements in the upper troposphere to characterize this variability. Seasonal humidity changes (Inamdar and Ramanathan, 1998) derived from the NASA Water Vapor Project data (Randel *et al.*, 1996) reveal a nearly unchanged relative-humidity level in the lower troposphere for the tropics whereas a significant moistening occurs in the mid to upper troposphere dominated by the deep convective regions of tropics. These results are also supported by the decadal-scale tropical humidity changes reported by Hense *et al.* (1988) and Flohn and Kapala (1989). Other studies, especially Schroeder and McGuire (1998) and Spencer and Braswell (1997) along with Lindzen *et al.* (1995) suggest that the drying in the arid regions is so overwhelmingly large as to more than offset the moistening elsewhere. Since these uncertainties are likely to prevail at least near term, it becomes more essential to turn to other diagnostic products like OLR and the atmospheric greenhouse effect measured from satellites to resolve the issue. The CERES instrument with its window channel (8–12  $\mu\text{m}$ ) is expected to aid significantly in this diagnostic study. This would enable us to partition the atmospheric greenhouse effect into contributions from the continuum, vibration–rotation, and pure rotation bands of water vapor.

### **5.6.2 Unresolved and emerging issues**

*Aerosol–cloud interactions.* In a fundamental sense, cloud drops are simply aerosols (an aerosol growing explosively in the presence of near-saturation relative humidity

becomes a cloud droplet). The fine-particle aerosol concentration is increasing significantly due to human activities and it is clear that cloud properties in the northern hemisphere are being altered. This increase is hypothesized to increase the number of cloud drops, suppress rainfall, and also decrease the daytime cloud fraction. We need a careful study of the cloud and aerosol forcing from satellite radiation-budget data to sort out these complex issues. The first step is to quantify the aerosol forcing at TOA from satellite data. New approaches have been proposed (Haywood *et al.*, 1999; Sathesh and Ramanathan, 2000) towards this goal. We also need to develop a better framework for sorting the data. For example, our ideas of clear skies and overcast skies in sorting the data may not hold under rigorous scrutiny. It is likely that a better approach is to think of the problem as varying from very low aerosol content (clear skies) to optically thick (overcast) aerosol content.

*Surface and atmospheric forcing.* We urgently need to extend the TOA forcing approach to consider the surface forcing and the atmospheric forcing individually. The so-called excess or anomalous absorption issue (resurrected recently by Cess *et al.*, 1995; Ramanathan *et al.*, 1995, and Pelewski and Valero, 1995, see Chapter 7) has highlighted the need for the surface forcing. What is the physics behind this excess absorption? None of the published studies to-date has identified the source for this excess absorption. Until we understand the physics for its source, we must remain skeptical. The main message to infer from the recent studies is that we lack accurate data to answer some fundamental questions. How much solar energy reaches the surface of the planet? How do clouds regulate the surface solar insulation? Considerable work is needed to develop radiation-budget instruments for surface-based measurements.

*Cloud feedback.* This is still an unresolved issue (see Chapter 8). The few results we have on the role of cloud feedback in climate change is mostly from GCMs. Their treatment of clouds is so rudimentary that we need an observational basis to check the model conclusions. We do not know how the net forcing of  $-18 \text{ W m}^{-2}$  will change in response to global warming. Thus, the magnitude as well as the sign of the cloud feedback is uncertain. Cloud radiative forcing effects are concentrated regionally (Figure 5.5). The data reveal three regions of major interest for future study.

- *Storm-track cloud systems over mid-latitude oceans.* These cloud systems associated with extra-tropical cyclones along with the persistent oceanic stratus, reflect more than 75% of solar radiation ( $C_s < -75 \text{ W m}^{-2}$ ), and contribute about 60% of the  $-18 \text{ W m}^{-2}$  net global cloud radiative forcing (Weaver and Ramanathan, 1997). Anthropogenic activities can directly perturb the radiative forcing of these clouds. The emission of anthropogenic  $\text{SO}_2$  and its subsequent conversion to sulfate aerosols can increase the number of cloud drops, which can enhance the shortwave cloud forcing by as much as  $-5$  to  $-10 \text{ W m}^{-2}$  (Kiehl and Briegleb, 1993).

- *Deep convective cloud systems in the tropics.* Maxima in  $C_1$  and in  $C_s$  of 60 to 100  $\text{W m}^{-2}$  (Figure 5.5) are found over the convectively disturbed regions of the tropics, including the tropical western Pacific, eastern equatorial Indian Ocean, equatorial rain-forest regions of South America and Africa. These cloud systems have been linked with a number of important climate feedback effects including the western Pacific warm pool cirrus thermostat (Ramanathan and Collins, 1991), cirrus albedo effect on global warming (Meehl and Washington, 1993) and increased convective-cirrus cloudiness with a tropical warming (Wetherald and Manabe, 1988; Mitchell and Ingram, 1992).
- *Marine stratocumulus coastal and sub-tropical cloud systems.* These sub-tropical cloud systems also contribute more than 75  $\text{W m}^{-2}$  to  $C_s$  and extend as far as 1000 km from the western coasts of North America, South America, and South Africa. Cloudiness is shown to increase with increase in low-level static stability (Klein *et al.*, 1993). Furthermore, the effect of sulfate aerosols in enhancing the cloud albedo is expected to be large for these low-level cloud systems.

## References

- Arrhenius, S. (1896). On the influence of carbonic acid in the air upon the temperature of the ground. *Phil. Mag.* **41**, 237–76.
- Augustsson, T. and V. Ramanathan (1977). A radiative-convective model study of the  $\text{CO}_2$  climate problem. *J. Atmos. Sci.* **34**, 448–51.
- Barkstrom, B. R. (1984). The Earth Radiation Budget Experiment (ERBE). *Bull. Amer. Meteor. Soc.* **65**, 1170–85.
- Cess, R. D. (1971). A radiative transfer model for planetary atmospheres. *J. Quant. Spectrosc. Radiat. Transfer* **11**, 1699–710.
- (1974). Radiative transfer due to atmospheric water vapor: global considerations of the Earth's energy balance. *J. Quant. Spectrosc. Radiat. Transfer* **14**, 861–71.
- (1975). Global climate change: an investigation of atmospheric feedback mechanisms. *Tellus* **27**, 193–8.
- (1976). Climate change: an appraisal of atmospheric feedback mechanisms employing zonal climatology, *J. Atmos. Sci.* **33**, 1831–43.
- (1982). The thermal structure within the stratospheres of Venus and Mars. *Icarus* **17**, 561–9.
- Cess, R. D. and S. Khetan (1973). Radiative transfer within the atmospheres of the major planets. *J. Quant. Spectrosc. Radiat. Transfer* **13**, 995–1009.
- Cess, R. D. and V. Ramanathan (1972). Radiative transfer in the atmosphere of Mars and that of Venus above the cloud deck. *J. Quant. Spectrosc. Radiat. Transfer* **12**, 933–45.
- Cess, R. D. and S. N. Tiwari (1972). Infrared radiative energy transfer in gases. In *Advances in Heat Transfer*, New York, NY, Vol. 8, pp. 229–82.
- Cess, R. D., G. L. Potter, J. P. Blanchet *et al.* (1989). Interpretation of cloud-climate feedback as produced by 14 atmospheric general circulation models. *Science* **245**, 513–16.
- (1990). Intercomparison and interpretation of climate feedback processes in nineteen atmospheric general circulation models. *J. Geophys. Res.* **95**, 16,601–16,615.
- Chamberlin, T. C. (1899). An attempt to frame a working hypothesis of the cause of glacial periods on an atmospheric basis. *J. Geol.* **7**, 609–21.

- Clough, S. A., F. X. Kneizys, and R. W. Davies (1989). Line shape and the water vapor continuum. In *IRS '88: Current Problems in Atmospheric Radiation*.
- (1992). Line shape and the water vapor continuum. *Atmos. Res.* **23**, 229–41.
- Collins, W. D., W. C. Conant, and V. Ramanathan (1994). Earth Radiation Budget, Clouds and Climate Sensitivity. In *The Chemistry of the Atmosphere: its Impact on Global Change*, ed. Jack, G. Calvert, Oxford, Blackwell Scientific Publishers, pp. 207–15.
- Drayson, S. R. (1967). Atmospheric transmission in the CO<sub>2</sub> bands between 12 m and 18 m. *Appl. Opt.* **5**, 385–91.
- Elsaesser, W. M. (1942). *Heat Transfer by Infrared Radiation in the Atmosphere*. Harvard Meteorological Studies 6, Cambridge, MA, Harvard University Press.
- Flohn, H. and A. Kapala (1989). Changes in tropical sea–air interaction processes over a 30-year period. *Nature* **338**, 244–5.
- Fourier, J.-B. J. (1827). Mémoire sur les Températures du Globe Terrestre et des Espaces Planétaires. *Mem. l'Inst. Fr.* **7**, 570–604.
- Goody, R. M. (1964). *Atmospheric Radiation I: Theoretical Basis*. London, Clarendon Press.
- Hallberg, R. and A. K. Inamdar (1993). Observation of seasonal variations of atmospheric greenhouse trapping and its enhancement at high sea surface temperature. *J. Clim.* **6**, 920–31.
- Harrison, E. F., P. Minnis, B. R. Barkstrom *et al.* (1990). Seasonal variation of cloud radiative forcing derived from the Earth Radiation Budget Experiment. *J. Geophys. Res.* **95**, 18687–703.
- Hartmann, D. L., V. Ramanathan, A. Berroir, and G. E. Hunt (1986). Earth radiation budget data and climate research. *Rev Geophys.* **24**, 439–68.
- Haywood, J. M., V. Ramaswamy, and B. J. Soden (1999). Tropospheric aerosol climate forcing in clear-sky satellite observations over the oceans. *Science* **283**, 1299–303.
- Hense, A., P. Krahe, and H. Flohn (1988). Recent fluctuations of tropospheric temperature and water vapor content in the tropics. *Meteorol. Atmos. Phys.* **38**, 215–27.
- Hitschfeld, W. and J. T. Houghton (1961). Radiative transfer in the lower stratosphere due to the 9.6 micron band of ozone. *Quart. J. Roy. Meteor. Soc.* **87**, 562–77.
- Inamdar, A. K. and V. Ramanathan (1994). Physics of greenhouse effect and convection in warm oceans. *J. Climate* **5**, 715–31.
- (1998). Tropical and global scale interactions among water vapor, atmospheric greenhouse effect, and surface temperature. *J. Geophys. Res.* **103**, 177–94.
- IPCC (1995). *The Science of Climate Change*. Cambridge, Cambridge University Press.
- Kaplan, L. D. (1959). A method for calculation of infrared flux for use in numerical models of atmospheric motion. *The Atmosphere and the Sea in Motion*. New York, NY, Rockefeller Institute Press, pp. 170–77.
- (1960). The influence of CO<sub>2</sub> variations on the atmosphere heat balance. *Tellus* **12**, 204–8.
- Kiehl, J. T. (1994). On the observed near cancellation between longwave and shortwave cloud forcing in tropical regions. *J. Clim.* **7**, 559–65.
- Kiehl, J. T. and B. P. Briegleb (1993). The relative roles of sulphate aerosols and greenhouse gases in climate forcing. *Science* **260**, 311–14.
- Kiehl, J. T. and V. Ramanathan (1983). CO<sub>2</sub> radiative parameterization used in climate models: comparison with narrow band models and with laboratory data. *J. Geophys. Res.* **88**, 5191–202.
- Langley, S. P. (1884). Researches on solar heat and its absorption by the Earth's atmosphere. *A Report of the Mount Whitney Expedition*. Professional Papers of the Signal Service No. 15, Washington, Government Printing Office.

- (1889). The temperature of the moon. *Mem. Nat'l. Acad. Sci.* **4**, Part II, 107–212.
- Lindzen, R. S. (1990). Some coolness concerning global warming. *Bull. Amer. Meteor. Soc.* **71**, 288–99.
- Lindzen, R. S., B. Kirtman, D. Kirk-Davidoff, and E. K. Schneider (1995). Seasonal surrogate for climate. *J. Clim.* **8**, 1681–4.
- Luther, F. M., R. G. Ellingson, Y. Fourquart *et al.* (1988). Intercomparison of radiation codes in climate models (ICRCCM): longwave clear-sky results – A workshop summary. *Bull. Amer. Meteor. Soc.* **69**, 40–8.
- Manabe, S. and R. F. Strickler (1964). On the thermal equilibrium of the atmosphere with a convective adjustment. *J. Atmos. Sci.* **21**, 361–85.
- Manabe, S. and R. T. Wetherald (1967). Thermal equilibrium of the atmosphere with a given distribution of relative humidity. *J. Atmos. Sci.* **24**, 241–59.
- McClatchey, R. A., W. S. Benedict, S. A. Clough *et al.* (1973). AFCRL atmospheric absorption line parameters compilation. Bedford, MA, Air Force Cambridge Research Laboratory, Report AFCRL-TR-73-0096.
- Meehl, G. A. and W. M. Washington (1995). Cloud albedo feedback and the super greenhouse effect in a global coupled GCM. *Clim. Dyn.* **11**, 399–411.
- Michelson, A. A. (1895). On the broadening of spectral lines. *Astrophys. J.* **2**, 251–61.
- Mitchell, J. F. B. and W. J. Ingram (1992). Carbon dioxide and climate – mechanisms of changes in cloud. *J. Clim.* **5**, 5–21.
- Möller, F. (1963). On the influence of changes in CO<sub>2</sub> concentration in air on the radiation balance of Earth's surface and on climate. *J. Geophys. Res.* **68**, 3877–86.
- Ohmura, A. and H. Gilgen (1993). Re-evaluation of the global energy balance. *Geophys. Monogr.* **75**, IUGG15: 93–110.
- Ramanathan, V. (1981). The role of ocean–atmosphere interactions in the CO<sub>2</sub> climate problem. *J. Atmos. Sci.* **38**, 918–30.
- (1987). The role of Earth radiation budget studies in climate and general circulation research. *J. Geophys. Res.* **92**, 4075–95.
- Ramanathan, V. and W. Collins (1991). Thermodynamic regulation of ocean warming by cirrus clouds deduced from observations of the 1987 El Niño. *Nature* **351**, 27–32.
- Ramanathan, V., R. D. Cess, E. F. Harrison *et al.* (1989). Cloud-radiative forcing and climate: results from the earth radiation budget experiment. *Science* **243**, 57–63.
- Randel, D. L., T. H. Vonder Haar, M. A. Ringerud *et al.* (1996). A new global water vapor dataset. *Bull. Amer. Meteor. Soc.* **77**, 1233–46.
- Raval, A. and V. Ramanathan (1989). Observational determination of the greenhouse effect. *Nature* **342**, 758–61.
- Revercomb, H. E., H. Buijs, H. B. Howell *et al.* (1988). Radiometric calibration of IR Fourier transform spectrometers: solution to a problem with the high-spectral resolution Interferometer Sounder. *Appl. Opt.* **27**, 3210–18.
- Roberts, R. E., L. M. Biberman, and J. E. A. Selby (1976). Infrared continuum absorption by atmospheric water vapor in the 8–10 μ window. *Appl. Opt.* **15**, 2085–90.
- Rothman L. S., R. R. Gamache, A. Golman *et al.* (1987). The HITRAN database. *Appl. Opt.* **26**, 4058–97.
- Salisbury, J. W. and D. M. D' Aria (1992). Emissivity of terrestrial materials in the 8–14 micron atmospheric window. *Remote Sens. Environ.* **42**, 83–106.
- Satheesh, S. K. and V. Ramanathan (2000). Large differences in tropical aerosol forcing at the top of the atmosphere and Earth's surface. *Nature* **405**, 60–3.
- Schneider, E. K., B. P. Kirtman, and R. S. Lindzen (1999). Tropospheric water vapor and climate sensitivity. *J. Atmos. Sci.* **56**, 1649–58.

- Schneider, S. H. (1972). Cloudiness as a global climate feedback mechanism: the effects of a radiation balance and surface temperature of variations in cloudiness. *J. Atmos. Sci.* **29**, 1413–22.
- Schroeder, S. R. and J. P. McGuire (1998). Widespread tropical atmospheric drying from 1979 to 1995. *Geophys. Res. Lett.* **25**, 1301–4.
- Shine, K. P. and A. Sinha (1991). Sensitivity of the Earth's climate to height-dependent changes in the water vapour mixing ratio. *Nature* **354**, 382–4.
- Soden, B. J. (1997). Variations in the tropical greenhouse effect during El Niño. *J. Climate* **10**, 1050–5.
- Soden, B. J. and S. R. Schroeder (2000). Decadal variations in tropical water vapor: a comparison of observations and a model simulation. *J. Clim.* **13**, 3337–41.
- Spencer, R. W. and W. D. Braswell (1997). How dry is the tropical free troposphere? Implications for global warming theory. *Bull. Amer. Meteor. Soc.* **78**, 1097–1106.
- Stephens, G. L. (1990). On the relationship between water vapor over the oceans and sea surface temperature. *J. Clim.* **3**, 634–45.
- Stephens, G. L. and T. J. Greenwald (1991). The Earth's radiation budget and its relation to atmospheric hydrology. 1. Observations of the clear sky greenhouse effect. *J. Geophys. Res.* **96**, 15311–24.
- Stephens, G. L. and P. J. Webster (1979). Sensitivity of radiative forcing to variable cloud and moisture. *J. Atmos. Sci.* **36**, 1542–56.
- Tyndall, J. (1861). On the absorption and radiation of heat by gases and vapours, and on the physical connexion of radiation, absorption, and conduction. *Philosophical Magazine* **22**, 169–94, 273–85.
- Waliser, D. E., N. E. Graham, and C. Gautier (1993). Comparison of the highly reflective cloud and outgoing longwave radiation datasets for use in estimating tropical deep convection. *J. Clim.* **6**, 331–53.
- Weaver, C. P. and V. Ramanathan (1997). Relationships between large-scale vertical velocity, static stability, and cloud radiative forcing over northern hemisphere extratropical oceans. *J. Clim.* **10**, 2871–87.
- Wetherald, R. T. and S. Manabe (1988). Cloud feedback processes in a general-circulation model. *J. Atmos. Sci.* **45**, 1397–1415.